Separation and Purification Technology 390 (2026) 137008

Contents lists available at ScienceDirect

Separation and Purification Technology

journal homepage: www.elsevier.com/locate/seppur

Efficient synthesis of covalent triazine frameworks from malononitrile-functionalized conjugated microporous polymer for multifunctional synergistic electrocatalytic hydrogen evolution, CO_2 recognition and separation

Mohamed Gamal Mohamed [a,b,*], Nian-Ping Chen [a], Tapomay Mondal [a], Shiao-Wei Kuo [a,c,*]

[a] Department of Materials and Optoelectronic Science, Center for Functional Polymers and Supramolecular Materials, National Sun Yat-Sen University, Kaohsiung 804, Taiwan
[b] Department of Chemistry, Faculty of Science, Assiut University, Assiut 71515, Egypt
[c] Department of Medicinal and Applied Chemistry, Kaohsiung Medical University, Kaohsiung 807, Taiwan

ARTICLE INFO

Editor: Dr. S Shouliang Yi

Keywords:
Conjugated microporous polymers
Covalent triazine frameworks
CO_2 capture
Ruthenium coordination
Electrocatalytic H_2 production

ABSTRACT

Carbon dioxide (CO_2) capture and hydrogen evolution reaction (HER) electrocatalysis represent two pivotal technologies addressing the urgent global challenges of carbon mitigation and sustainable energy transition. Rationally designing porous organic materials with high surface area, tunable pores, and accessible active sites enhances both adsorption and catalytic performance. In this work, we report a tailored conjugated microporous polymer (CMP), PF-CN CMP, synthesized via the introduction of cyano groups into the monomer 2-(2,7-dibromo-9H-fluoren-9-ylidene)malononitrile (FL-2CN-2Br), followed by coupling with 1,3,6,8-tetraethynylpyrene (Py-T) through a Sonogashira cross-coupling reaction. The resulting CMP was subsequently transformed into covalent triazine frameworks (CTFs) with well-defined triazine rings through an ionothermal reaction with anhydrous $ZnCl_2$. By tuning the PF-CN CMP/$ZnCl_2$ weight ratios [1:5 and 1:10] and reaction temperature [400 and 500 °C] to afford PFCTF materials exhibiting high specific surface areas (up to 1204.8 $m^2\ g^{-1}$) and exceptional thermal stability (T_{d10} up to 660 °C). Among them, PFCTF-10-500 displayed CO_2 uptake of 5.73 mmol g^{-1} at 273 K and 1 bar, with excellent reproducibility and selectivity. Furthermore, HER activity under alkaline conditions was markedly enhanced by coordinating Ru^{3+} ions to the pyridinic nitrogen sites within the PFCTFs network, yielding Ru@PFCTF-10-500 with a low overpotential of just 89 mV and long-term operational stability.

1. Introduction

Rapid industrialization has significantly increased greenhouse gas emissions, intensifying global environmental challenges such as climate change, sea-level rise, and ecosystem disruption [1–6]. CO_2 is the dominant contributor, accounting for over 76% of total emissions according to the IPCC [7–8]. In response, global CO_2 capture, utilization, and storage (CCUS) efforts aim to exceed 100 million tons of annual CO_2 storage by 2030 [9–11], while the European Union has committed to reducing greenhouse gas emissions by at least 55% relative to 1990 levels by 2030 in line with the Paris Agreement [12–15]. Achieving these targets requires the transition to clean and sustainable energy systems. Hydrogen (H_2) is a promising energy carrier due to its zero CO_2 emissions upon combustion and high gravimetric energy density (120–140 MJ kg^{-1}), making it particularly suitable for hard-to-electrify sectors such as transportation and heavy industry [16–18]. Among available production routes, water electrolysis is regarded as an effective strategy for sustainable H_2 generation [19–20]. However, its large-scale implementation is hindered by the reliance on costly noble-metal electrocatalysts [21–22], motivating the development of efficient alternatives such as transition metal compounds [23–25], carbon-based materials [26–27], CMPs [28–34], and MOF-derived catalysts [35–37].

Simultaneously, solid-state CO_2 capture using porous adsorbents has emerged as a reversible and cost-effective approach to mitigate emissions, while electrochemical hydrogen evolution reaction (HER) enables clean energy conversion [38–44]. Both processes critically depend on

* Corresponding authors at: Department of Materials and Optoelectronic Science, Center for Functional Polymers and Supramolecular Materials, National Sun Yat-Sen University, Kaohsiung 804, Taiwan.
E-mail addresses: mgamal.eldin12@yahoo.com, mgamal.eldin12@mail.nsysu.edu.tw (M.G. Mohamed), kuosw@faculty.nsysu.edu.tw (S.-W. Kuo).

https://doi.org/10.1016/j.seppur.2026.137008
Received 5 September 2025; Received in revised form 24 December 2025; Accepted 21 January 2026
Available online 24 January 2026

advanced porous materials with high surface area, tunable porosity, and accessible active sites [45,46]. Conjugated microporous polymers (CMPs) have attracted growing interest due to their structural diversity and potential in gas adsorption and electrocatalysis [47–52]. Nevertheless, challenges such as limited CO_2 uptake at low pressures, insufficient selectivity, poor electrical conductivity, and restricted active-site accessibility remain [43–47]. Addressing these limitations requires the rational design of next-generation CMP-based frameworks with enhanced stability, charge transport, and tailored surface chemistry to enable efficient dual functionality in CO_2 capture and H_2 evolution.

Previous studies on CMPs have shown that their pores primarily originate from the gaps between crosslinking points and the voids created by the stacking of conjugated planar units [47–52]. This arrangement produces an unordered yet stable microporous network, whose properties can vary depending on the degree of monomer crosslinking and the steric hindrance imposed by rigid structural motifs [47–52]. For instance, in earlier work, a CMP synthesized from pyrene (Py) and fluorene (FL) via a Sonogashira coupling reaction exhibited a relatively low specific surface area [53]. Building on this, the present study exploits the tunability of the 9,9-position of the FL unit by introducing cyano groups into the monomer, which is subsequently polymerized into a cyano-functionalized CMP. Under ionothermal conditions, the C≡N groups undergo cyclotrimerization, converting the CMP into a covalent triazine frameworks (CTFs). In ionothermal synthesis, the high temperatures required can induce partial carbonization; therefore, a pre-crosslinked CMP precursor is employed here to mitigate carbonization during the thermal conversion process. CTFs have found wide applications in gas storage, heterogeneous catalysis, oxygen reduction reaction (ORR) electrocatalysis, CO_2 capture and conversion, and energy storage [53–57]. Their excellent CO_2 adsorption capabilities are attributed to the synergistic effect of heteroatoms within the triazine ring and the high surface area afforded by their crosslinked frameworks. For example, Chen et al. synthesized four Py-based CTFs that achieved CO_2 uptakes of up to 104.9 $cm^3\ g^{-1}$ at 273 K [58]. Similarly, Zhao et al. reported a sp^2 carbon-conjugated covalent organic framework (COF) with a triazine core, which was coordinated with ruthenium ions to yield Ru@COF-1. This material exhibited a large specific surface area and well-defined porous channels, promoting efficient interaction between reactants and active sites, and delivered an overpotential of approximately 200 mV at a current density of 10 mA cm^{-2} [59].

Building upon prior advancements in CTFs synthesis via ionothermal methods, this study utilizes Py–CN CMP synthesized through the Sonogashira coupling of Py-T with FL-2CN-2Br—as a precursor to fabricate novel PFCTF materials. These frameworks were synthesized under high-temperature conditions of 400 °C and 500 °C, employing molten $ZnCl_2$ at two distinct weight ratios (1:5 and 1:10). At these elevated temperatures, $ZnCl_2$ remains in a molten state, allowing deep infiltration into the polymer matrix, activation of intermolecular C≡N bonds, and coordination with nitrile groups to drive efficient cyclotrimerization into triazine rings. This process concurrently induces secondary cross-linking within the polymer network, markedly enhancing the structural integrity and elevating the specific surface area of the resulting PFCTF materials. The synthesized PFCTFs were thoroughly characterized to elucidate their chemical composition, elemental distribution, thermal stability, crystallinity, surface area, and pore morphology. Their performance in CO_2 adsorption was rigorously evaluated. To further augment their functionality for electrocatalytic H_2 evolution reactions (HER), Ru^{3+} ions were incorporated into the PFCTF framework. The strong metal–ligand coordination introduced additional catalytically active sites, significantly boosting the electrocatalytic efficiency.

2. Experimental section

2.1. Materials

Bromine (Br_2, 98%), triethylamine (Et_3N, 99.5%), tetrakis (triphenylphosphine)palladium(0) ($Pd(PPh_3)_4$, 99%), sodium sulfite (Na_2SO_3, 98%), 2,7-dibromofluorene [2,7-FL-2Br, 97%], ruthenium (III) acetate [$Ru(CH_3COO)_3$, 95%], dimethyl sulfoxide (DMSO), malononitrile (99%), acetonitrile, ethanol (EtOH), toluene, triphenylphosphine (PPh_3, 99%), copper(I) iodide (CuI, ≥99.5%), trimethylsilylacetylene (TMSA, 99%), dichloromethane (DCM), methanol, potassium carbonate (K_2CO_3, ≥99%), dimethylformamide (DMF), zinc chloride ($ZnCl_2$, ≥98%), hydrogen chloride (HCl, 37%) were received from Alfa Aesar, Acros and Sigma-Aldrich. Py-T was prepared following the methods described in previous studies [60–63].

2.2. Synthesis of FL-2CN-2Br

A solution of chromium oxide (Cr_2O_3, 10%) in CH_3COOH (60 mL) was added slowly to a solution of 2,7-FL-2Br (6 g, 18.6 mmol) in CH_3COOH (60 mL), and the reaction mixture was stirred for 8 h. The reaction mixture was brought to neutral pH using aqueous $NaHCO_3$ (500 mL). The formed yellow solid was isolated, rinsed with water, and recrystallized from a mixture of ethanol and toluene to obtain 2,7-dibromofluoren-9-one [2,7-FO-2Br, 5.14 g, 86%] as a yellow solid. FTIR [cm^{-1}, **Fig. S1**]: 3083, 1721 (C=O), 1591(C=C), 681. ^{1}H NMR (600 MHz, $CHCl_3$-d, δ, ppm, **Fig. S2**): 7.72 (2H) 7.59 (2H) 7.35 (2H). ^{13}C NMR (125 MHz, $CHCl_3$-d, δ, ppm, **Fig. S3**): 190.74, 142.04, 137.71, 135.34, 127.63, 123.62,121.57. 2,7-FO-2Br (4.16 g, 12.3 mmol) was dissolved in DMSO (50 mL), and malononitrile (1.76 g, 26.64 mmol) was added and reacted at 110 °C for 12 h. After reaction, the original yellow color will change to red, filtered and washed with acetonitrile, THF, and acetone, and dried to obtain red powder [3.5 g, 84.13%]. FTIR [cm^{-1}]: 3092, 2225 (C≡N), 1565, 585. ^{1}H NMR (600 MHz, $CHCl_3$-d, δ, ppm, **Fig. S4**): 8.5 (2H) 7.66 (2H) 7.42 (2H).

2.3. Synthesis of PF-CN CMP

A mixture of Py-T (0.17 g, 0.57 mmol), FL-2CN-2Br (0.44 g, 1.14 mmol), CuI (0.011 g, 0.06 mmol), PPh_3 (0.015 g, 0.06 mmol), and Pd $(PPh_3)_4$ (0.07 g, 0.06 mmol) was placed in a round-bottom flask, followed by the addition of DMF (10 mL) and Et_3N (10 mL) under an inert atmosphere. The reaction mixture was stirred at 90 °C for 72 h. Upon completion, the resulting precipitate was collected by filtration and thoroughly washed with THF, methanol, and acetone to afford a red solid [0.14 g, 82.4%].

2.4. Synthesis of PFCTFs [PFCTF-5-400, PFCTF-10-400, PFCTF-5-500 and PFCTF-10-500]

Four PFCTF samples were prepared by mixing the as-synthesized PF-CN CMP with anhydrous $ZnCl_2$ at weight ratios of 1:5 [PF-CN CMP (0.1 g): $ZnCl_2$ (0.5 g)] or 1:10 [PF-CN CMP (0.1 g): $ZnCl_2$ (1 g)]. The mixtures were sealed under a nitrogen (N_2) atmosphere and subjected to ionothermal treatment at either 400 or 500 °C for 72 h. After cooling to room temperature, the resulting black solids were ground into a fine powder and subjected to sequential soaking in 1 M HCl (400 mL), deionized water, and acetone for 1 day to remove residual salts and impurities. The purified products were obtained as black, powdery PFCTFs.

2.5. Preparation of Ru@PFCTFs

PFCTFs (0.10 g) were dispersed in anhydrous methanol (10 mL), followed by the addition of $Ru(CH_3COO)_3$ (0.05 g). The suspension was stirred continuously at room temperature for 12 h to allow sufficient incorporation of Ru species into the framework. After the treatment, the solid product was collected, thoroughly rinsed with methanol and acetone to remove residual precursors, and then dried in an oven to yield the Ru@PFCTFs composite. The loading amount of Ru in PFCTF-5-400, PFCTF-10-400, PFCTF-5-500, and PFCTF-10-500 was quantified by ICP-

OES to be 8.52, 9.31, 8.74, and 9.67 wt%, respectively.

3. Results and discussion

3.1. Synthesis and structural characterization of PF-CN CMP

To achieve CTFs with a high crosslinking density and high surface area, PF-CN CMP was employed as the precursor. The synthesis route for

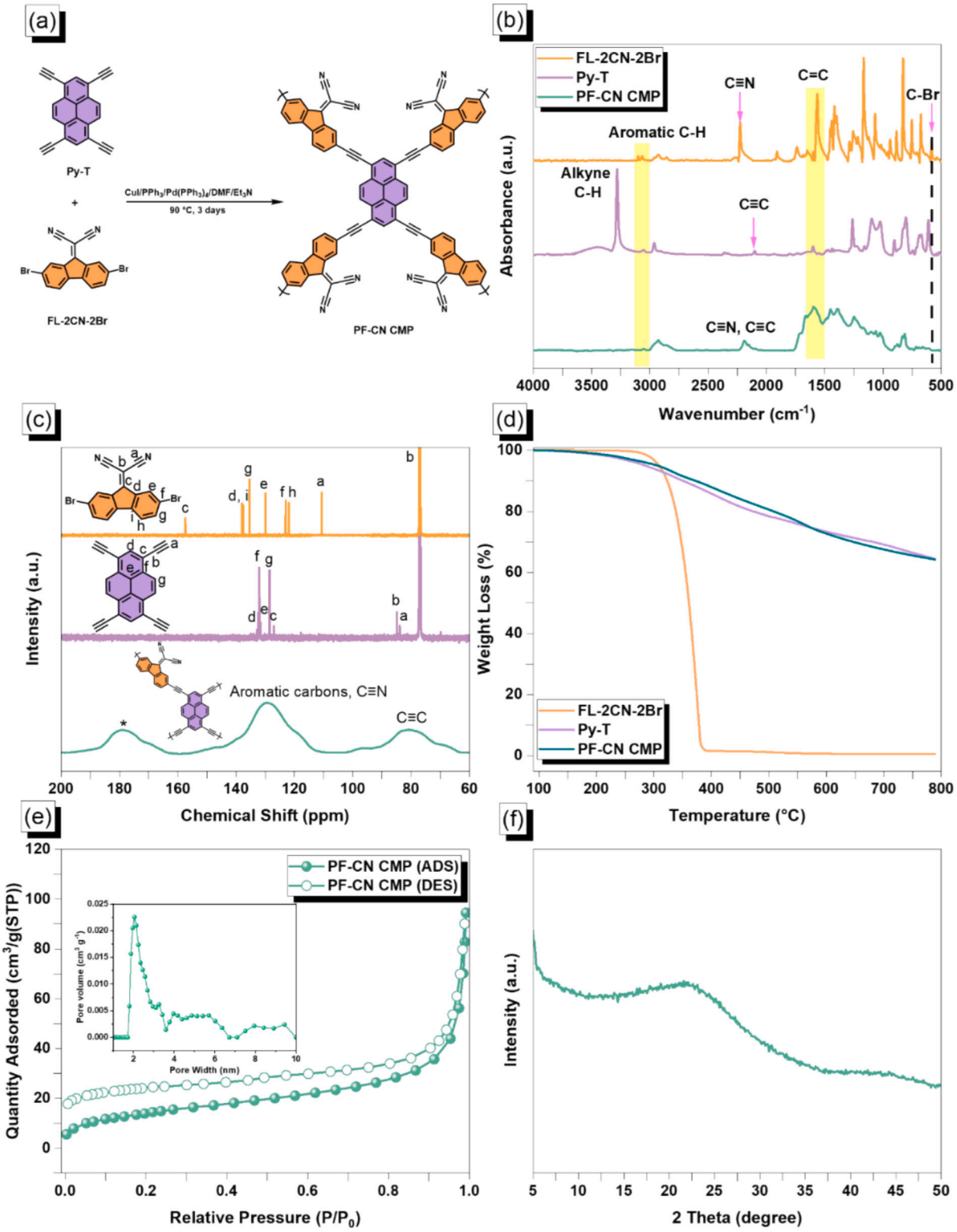

Fig. 1. (a) The preparation of PF-CN CMP, (b) FTIR, (c) ^{13}C NMR, (d) TGA of FL-2CN-2Br, Py-T and PF-CN CMP, (e) BET isotherm (inset: pore size distributions) and (f) XRD of PF-CN CMP.

PF-CN CMP, illustrated in Fig. 1(a), involves a palladium-catalyzed coupling reaction between Py-T and FL-2CN-2Br monomers in a DMF/Et_3N solvent system, yielding a red solid with excellent efficiency. To unequivocally confirm the successful formation of PF-CN CMP, Fourier transform infrared (FT-IR) and solid-state ^{13}C nuclear magnetic resonance (NMR) spectroscopy were conducted. These analyses were used to detect the transformation of functional groups from the individual monomers (Py-T and FL-2CN-2Br) to the polymerized PF-CN CMP, thereby verifying the progression and completion of the polymerization process. As shown in Fig. 1(b), the FTIR spectrum of FL-2CN-2Br displays characteristic absorption bands at 3092, 2225, 1565, and 585 cm^{-1}, corresponding to sp^2 aromatic C—H, nitrile (C≡N), aromatic C═C, and C—Br stretching vibrations, respectively [64]. In contrast, the Py-T monomer exhibits distinct peaks at 3279, 3052, and 2106 cm^{-1}, attributable to alkyne C—H, aromatic C—H, and C≡C bonds [60–63]. The FTIR spectrum of the synthesized PF-CN CMP reveals a prominent peak at 2190 cm^{-1}, assigned to the stretching vibrations of both C≡N and C≡C bonds, confirming their incorporation within the polymer framework. Additionally, the absorption band at 1599 cm^{-1} is attributed to aromatic C═C stretching, while the peak at 3058 cm^{-1} corresponds to aromatic C—H stretching. Notably, the significant reduction of the C—Br stretching band at 582 cm^{-1}, alongside the retention of aromatic C—H, nitrile, and alkyne signals, demonstrates the successful coupling reaction and corroborates the structural integrity of the PF-CN CMP. Furthermore, the solution ^{13}C NMR spectra of the FL-2CN-2Br and Py-T monomers, presented in Fig. 1(c), display aromatic carbon resonances ranging from 157.33 to 110.63 ppm and 131.97 to 126.9 ppm, respectively. Additional signals appear at 77.02 ppm in FL-2CN-2Br, corresponding to the C═C-$(CN)_2$ unit, and at 84.77 and 83.94 ppm in Py-T, attributed to the internal and external alkyne carbons. In the solid-state ^{13}C NMR spectrum of PF-CN CMP (Fig. 1(c)), the peaks between 142 and 121 ppm are assigned to aromatic C═C carbons, while the resonance at 81 ppm corresponds to the C≡C moiety. Moreover, the signal at 119 ppm confirms the presence of the nitrile (C≡N) functional group within the PF-CN CMP framework. As illustrated in Fig. 1(d), thermogravimetric analysis (TGA) was performed to evaluate the thermal stability of FL-2CN-2Br, Py-T monomers, and the synthesized PF-CN CMP. The decomposition temperature at 10% weight loss (T_{d10}) was found to be 323 °C for FL-2CN-2Br, 351 °C for Py-T, and significantly higher at 372 °C for Py-FL-2CN CMP. This progressive increase in T_{d10} highlights the superior thermal robustness imparted by the covalent polymer network in the PF-CN CMP structure compared to the individual monomers. Moreover, carbon residue yields measured at 800 °C were markedly different: FL-2CN-2Br showed an extremely low carbon yield of 0.56%, while Py-T and PF-CN CMP retained substantial carbon contents of 65% and 64%, respectively.

Following confirmation of the PF-CN CMP's successful synthesis, detailed pore structure analysis of PF-CN CMP was conducted using nitrogen adsorption-desorption isotherms, as shown in Fig. 1(e). The isotherm exhibited a type II adsorption profile, characteristic of non-porous or macroporous materials with limited microporosity. The specific surface area, calculated via the BET method, was relatively modest at 51.36 $m^2\ g^{-1}$. Pore size distribution analysis revealed pores predominantly in the mesoporous range, spanning 2.03 to 3.92 nm, with a total pore volume of 0.13 $cm^3\ g^{-1}$. Furthermore, the crystallinity of the PF-CN CMP was investigated by X-ray diffraction (XRD) analysis, presented in Fig. 1(f). The broad, featureless diffraction pattern indicates an amorphous structure lacking long-range order. The surface morphology of PF-CN CMP, as revealed by scanning electron microscopy (SEM) and transmission electron microscopy (TEM) images (**Fig. S5**), is characterized by aggregated spherical particles with an irregular and disordered arrangement. These micrographs highlight the lack of uniformity in shape and organization, indicating a complex, non-crystalline network structure typical of the synthesized PF-CN CMP.

3.2. Synthesis and characterization of PFCTFs [PFCTF-5-400, PFCTF-10-400, PFCTF-5-500 and PFCTF-10-500]

The synthesis of PFCTF materials—namely PFCTF-5-400, PFCTF-10-400, PFCTF-5-500, and PFCTF-10-500 was achieved via an ionothermal process, where PF-CN CMP was reacted with molten $ZnCl_2$ at two distinct temperatures, 400 °C and 500 °C under N_2 gas, as depicted in Fig. 2(a). To verify the formation of triazine rings following the ionothermal treatment of PF-CN CMP, FTIR spectroscopy was performed, as presented in Fig. 2(b). The FTIR spectra of the PFCTF samples reveal a gradual diminution and eventual disappearance of the cyano (C≡N) stretching peak around 2220 cm^{-1} with increasing thermal treatment, confirming the effective consumption of nitrile groups via cyclotrimerization. Simultaneously, new absorption bands emerge at 1485 and 1374 cm^{-1}, attributed to the C═N and C—N stretching vibrations characteristic of the triazine ring, thereby unequivocally confirming the successful transformation of C≡N functionalities into a triazine framework [65–67]. The relatively weak and broad nature of these signals likely results from partial carbonization at elevated.

temperatures and the restricted vibrational freedom imposed by the highly crosslinked polymer network. Complementary solid-state ^{13}C NMR analysis (Fig. 2(c)) further supports this transformation, showing a distinct resonance at approximately 174.5 ppm assigned to the carbon atoms within the triazine rings, alongside a broad peak at 129.33 ppm corresponding to aromatic carbons in the PFCTF frameworks. TGA analysis (Fig. 2(d)) demonstrates a marked enhancement in thermal stability after ionothermal treatment for the resulting PFCTF materials. Notably, the PFCTF-10-500 sample exhibits exceptional thermal resilience, with T_{d5} occurring at 453 °C and T_{d10} at 660 °C, accompanied by a high char yield of 84 wt%. These thermal properties reflect a highly robust, heat-resistant structure. Moreover, the increased degree of crosslinking and incorporation of triazine rings contributes significantly to the improved chemical stability and structural integrity of the PFCTFs. The PXRD patterns (**Fig. S6**) reveal a broad diffraction peak at $2\theta \approx 23°$, characteristic of the (002) plane and indicative of π–π stacking interactions between aromatic layers. In the samples PFCTF-5-500 and PFCTF-10-500, additional sharp peaks emerge around 41–43°, which can be attributed to the (100) and (101) planes, signifying the development of short-range ordered or graphitic-like domains [65–67]. The pronounced increase in peak intensity and sharpness with higher $ZnCl_2$ loading, particularly evident in PFCTF-10-500, demonstrates enhanced structural ordering facilitated by the combined effects of elevated synthesis temperature and $ZnCl_2$ concentration during ionothermal treatment. **Fig. S7** displays the Raman spectra of the PFCTF samples within the 1000–2600 cm^{-1}. All four PFCTFs feature two dominant peaks near 1350 cm^{-1} (D band) and 1596 cm^{-1} (G band), characteristic of graphitic structures. Notably, PFCTF-10-500 displays the highest I_D/I_G ratio of 0.87, indicating the richest presence of condensed aromatic domains and superior graphitization [66–67]. Following the successful synthesis of the PFCTFs, their porosity was rigorously assessed via nitrogen adsorption–desorption measurements conducted at 77 K, with results illustrated in **Figs. 3(a–d)**. According to IUPAC classification, all four PFCTFs display type I isotherms, characteristic of predominantly microporous architectures. The materials PFCTF-5-400, PFCTF-10-400, PFCTF-5-500, and PFCTF-10-500 exhibited impressive specific surface areas [S_{BET}] of 821, 1127, 871, and 1205 $m^2\ g^{-1}$, respectively. Notably, increasing the $ZnCl_2$ ratio during ionothermal synthesis markedly enhanced the surface area, reflecting $ZnCl_2$'s dual functionality as both a catalyst and templating agent. At elevated concentrations, $ZnCl_2$ facilitates the development of well-defined microporous networks and simultaneously stabilizes the framework during high-temperature polymerization, effectively preventing pore collapse and preserving structural integrity [65,68,69]. Furthermore, the pore diameters of PFCTF-5-400, PFCTF-10-400, PFCTF-5-500, and PFCTF-10-500 were 1.32–1.75, 0.99–1.94, 1.32–1.74, and 1.04–1.82 nm, with microporous characteristics, respectively. The chemical composition of the PFCTFs

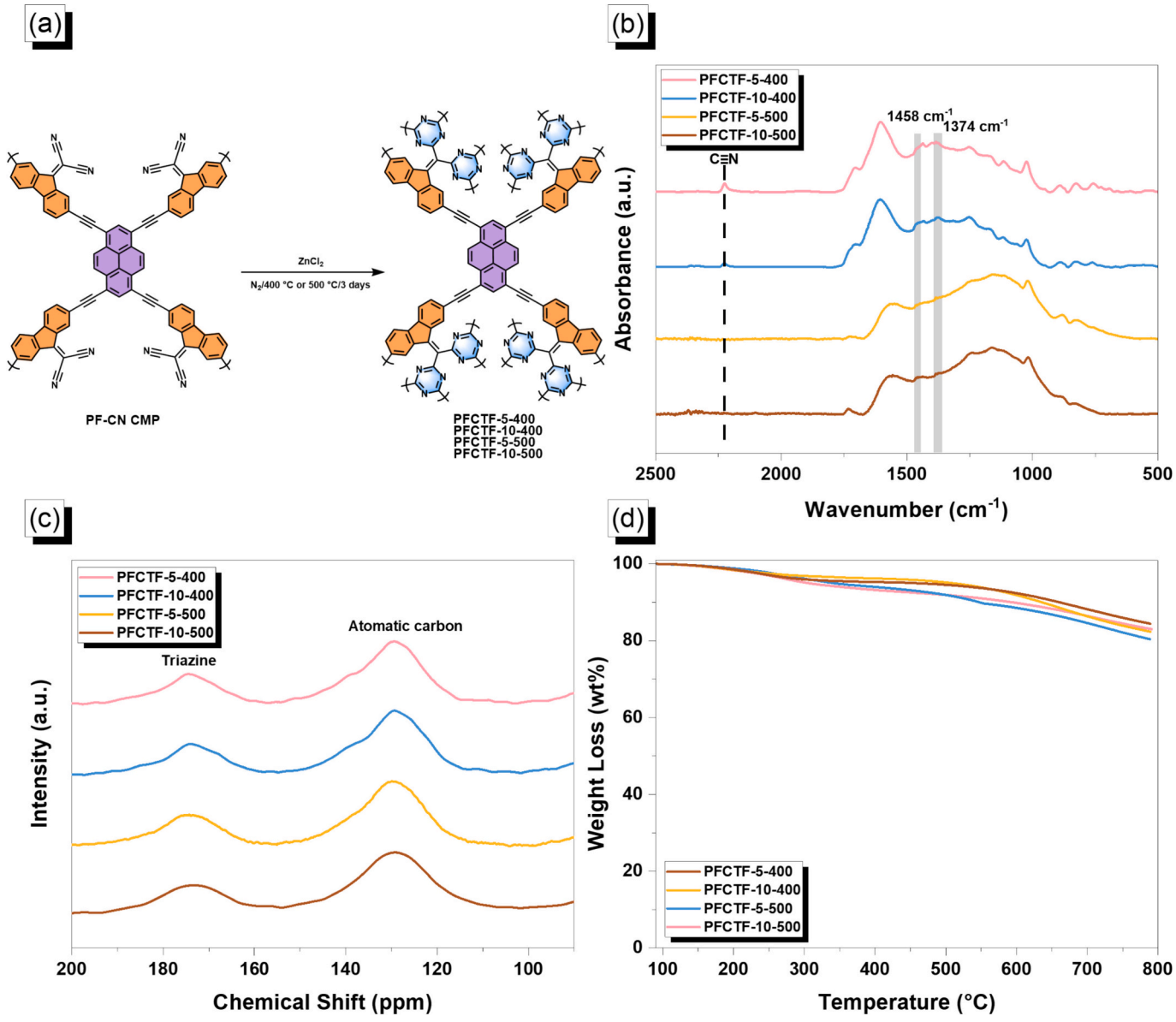

Fig. 2. (a) Preparation of PFCTF materials via the reaction of PF–CN CMP with anhydrous $ZnCl_2$ at 400 °C and 500 °C, (b) FTIR, (c) solid-state ^{13}C nuclear magnetic resonance (NMR) spectroscopy, and (d) TGA of PFCTF materials.

was further elucidated by X-ray photoelectron spectroscopy (XPS), with high-resolution N 1 s spectra presented in Figs. 3**(e–h)**. Peak deconvolution identified three distinct nitrogen species at binding energies near 398.0 eV, 399.5 eV, and 401.0 eV, assigned to pyridinic nitrogen, pyrrolic nitrogen, and graphitic (quaternary) nitrogen, respectively, and the percentage of pyridinic nitrogen, pyrrolic nitrogen, and graphitic (quaternary) nitrogen in all PFCTFs is summarized in **Table S1**. **Table S1** revealed that PFCTF-10-500 possesses the highest pyridinic nitrogen content among the PFCTF samples, underscoring its unique chemical environment and potential functional advantages. The surface morphologies of the PFCTFs were investigated using SEM, as depicted in Figs. 3**(i–l)**. In comparison to the PF-CN CMP precursor (**Fig. S5**), PFCTF-5-400 and PFCTF-10-400 maintain relatively similar spherical particle morphologies. Conversely, PFCTF-5-500 and PFCTF-10-500 exhibit distinctly more pronounced localized layered arrangements, resulting from carbonization induced by high-temperature treatment. PFCTF-5-500 exhibits a loosely arranged layered structure with smooth surfaces and indistinct pore features, suggesting insufficient pore development during synthesis. Conversely, PFCTF-10-500, synthesized with an increased $ZnCl_2$ content, presents a more compact and rugged morphology, characterized by a clearly discernible porous framework. SEM-EDS analysis [**Fig. S8**] confirmed the presence of carbon (C, yellow color) and nitrogen (N, green color) atoms in PF-CN CMP and all PFCTF samples, with their respective atomic percentages summarized in **Table S2**. Furthermore, TEM images (Figs. 3**(m–p)**) corroborate that the PFCTFs possess amorphous structural characteristics.

3.3. CO_2 adsorption performance of PFCTFs

Given the high specific surface area of the PFCTFs combined with nitrogen sites in the triazine rings that facilitate strong interactions with CO_2 (Fig. 4(a)), their CO_2 adsorption capacities were systematically evaluated. As illustrated in the adsorption isotherms (Figs. 4(b) and (c)), the obtained PFCTF framework samples with the greatest surface areas demonstrated superior CO_2 uptake. Notably, PFCTF-10-500 achieved an exceptional CO_2 adsorption capacity of 5.73 mmol g^{-1} at 273 K and 1 bar, positioning it among the top-performing CTFs reported under similar conditions [**Fig. S9** and **Table S3**]. Remarkably, this material

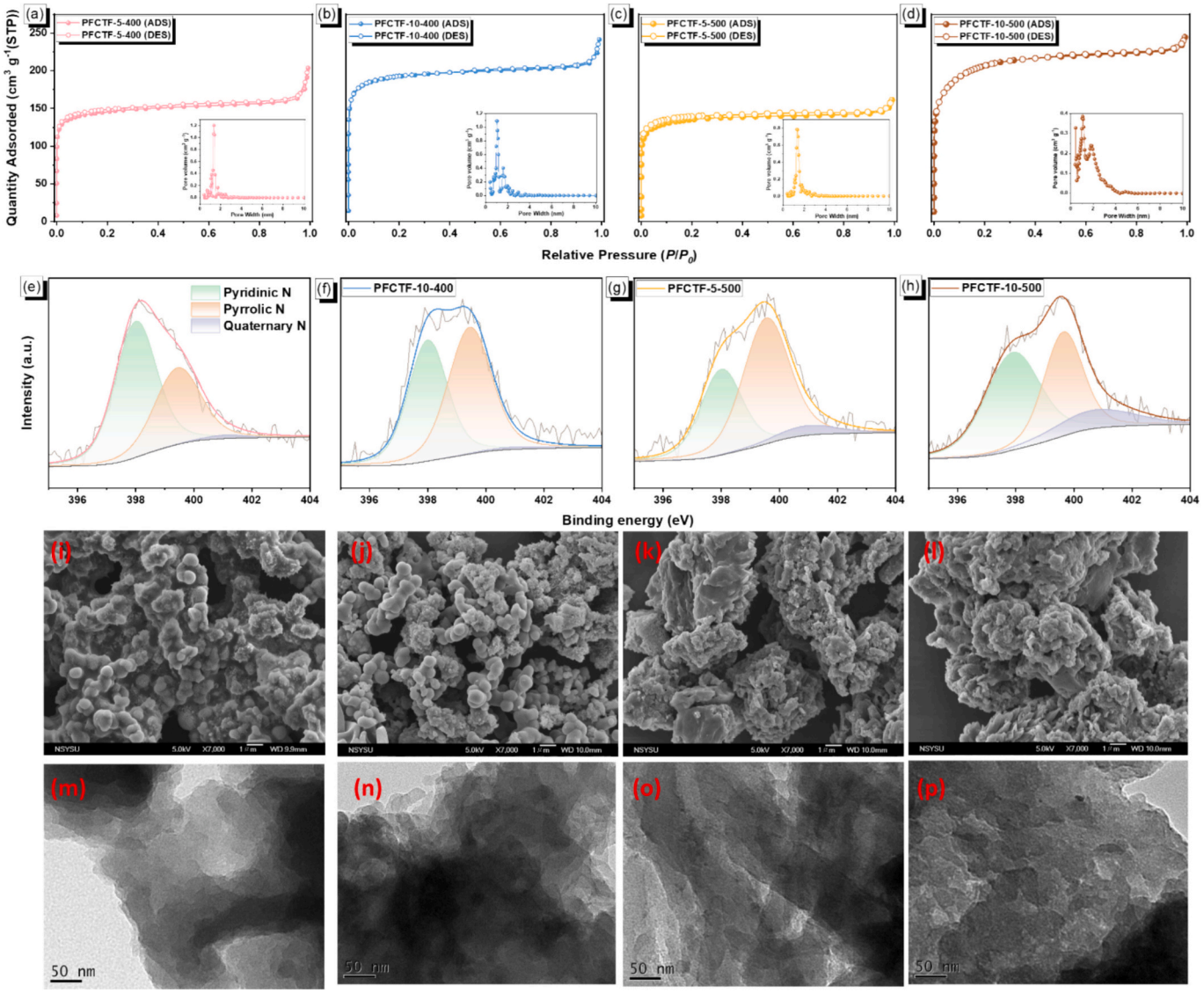

Fig. 3. (a-d) BET isotherm (inset: pore size distributions), (e-h) XPS spectra N1s, (i-l) SEM images, and (m-p) TEM images of (a, e, i, m) PFCTF-5-400, (b, f, j, n) PFCTF-10-400, (c, g, k, o) PFCTF-5-500 and (d, h, l, p) PFCTF-10-500.

also maintained impressive CO_2 capture efficiency at ambient temperature (298 K), with an uptake of 3.74 mmol g^{-1}. The superior CO_2 adsorption performance of PFCTF-10-500 relative to other PFCTF materials can be ascribed to its higher nitrogen content, particularly pyridinic nitrogen, which enhances specific interactions with CO_2, together with its large surface area [70–72]. Consistent with this interpretation, Vidal et al. demonstrated using nitrogen-doped nanorings that increasing nitrogen content raises the electron density of the framework, thereby strengthening the interaction between the adsorbent and CO_2 molecules [73].

To further elucidate the interactions governing CO_2 adsorption, the Clausius–Clapeyron equation was applied to the adsorption isotherms at 273 K and 298 K to determine the isosteric heat of adsorption (Q_{st}). As shown in Fig. 4(d), the Q_{st} values for the PFCTF materials at low coverage fall within the range of 25.3–27.1 kJ mol^{-1}, reflecting strong dipole–quadrupole electrostatic interactions between the polarizable CO_2 molecules and the nitrogen-rich PFCTF framework. The adsorption mechanism is predominantly physisorption, which offers the significant advantage of reversibility. Given that reusability is a key factor for practical deployment, the cycling performance of PFCTF-10-500 was evaluated over five consecutive adsorption–desorption cycles (Fig. 4(i)). The results reveal that the CO_2 uptake remained essentially unchanged, confirming the material's excellent stability and regeneration capability. Beyond CO_2 uptake and structural characteristics of the synthesized PFCTFs, the CO_2/N_2 adsorption selectivity is a critical parameter for assessing the performance of porous adsorbents. Using CO_2 and N_2 adsorption isotherms measured at identical temperatures, the CO_2/N_2 selectivity was calculated via the ideal adsorption solution theory (IAST) model (Figs. 4**(e–h)**). The evaluation was performed under simulated flue gas conditions (15% CO_2 and 85% N_2 at ~0.15 bar). As summarized in **Table S3**, the four PFCTFs exhibit comparable selectivity values, with noticeably higher selectivity at 273 K compared to 298 K. This temperature dependence reflects the predominance of physisorption in these PFCTF frameworks, as previously discussed. To assess performance under low-pressure conditions ($\leq$ 0.1 bar), relevant to atmospheric CO_2 concentrations, the Henry's law model was applied (**Fig. S10**). The calculated selectivities, along with corresponding numerical comparisons, are listed in **Table S3**. While the selectivity values of PFCTFs are not exceptionally high, the combination of reasonable CO_2/N_2 selectivity and substantial CO_2 adsorption capacity highlights their potential as viable materials for CO_2 capture and mitigation technologies.

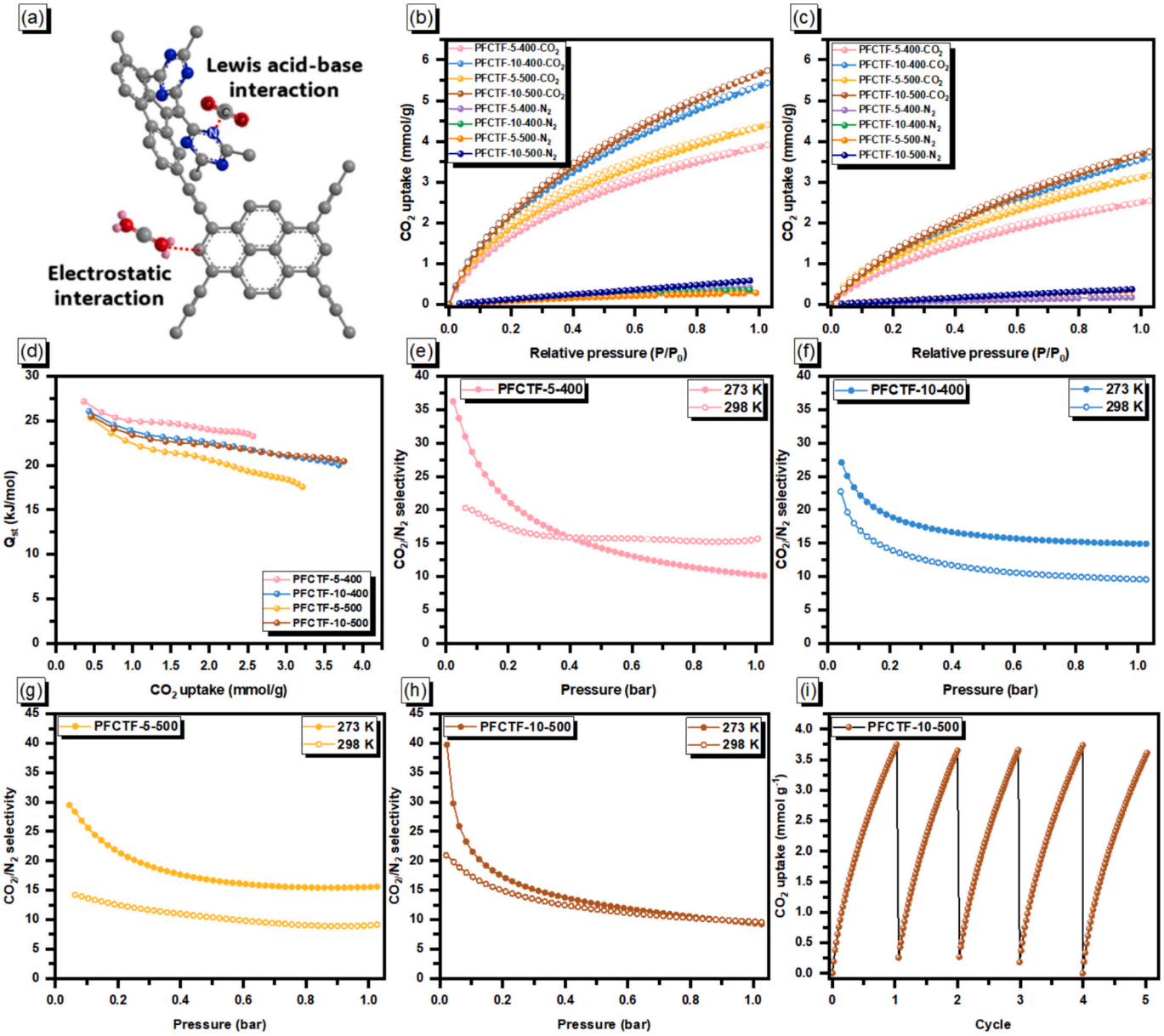

Fig. 4. (a) Proposed interaction mechanism between PFCTFs and CO_2 molecules. CO_2 and N_2 adsorption isotherms of PFCTFs at (a) 273 K and (c) 298 K. (d) Q_{st} values of PFCTFs. IAST selectivity ($S_{CO2/N2}$) of CO_2 /N_2 at 273 K and 298 K for (e) PFCTF-5-400, (f) PFCTF-10-400, (g) PFCTF-5-500, (h) PFCTF-10-500, and (i) five-cycle CO_2 adsorption performance of CTF-10-500 at 298 K.

3.4. Synthesis, characterization, and electrocatalytic HER of Ru^{3+} coordinated PFCTFs (Ru@PFCTFs)

To boost the electrocatalytic activity of PFCTF materials, Ru^{3+} metal ions were incorporated into the nitrogen-rich carbon framework containing triazine units, enabling coordination interactions (Fig. 5(a)). To elucidate the elemental composition and electronic states of the fabricated Ru@PFCTF-10-500 electrocatalyst, X-ray photoelectron spectroscopy (XPS) measurements were carried out. As shown in **Fig. S11**, the survey spectrum confirms the presence of C, N, O, and Ru elements in the composite. The high-resolution C 1 s, Ru 3d, Ru 3p and N 1 s spectra of Ru@PFCTF-10-500 are presented in Figs. 5**(b-d)**. The high-resolution C 1 s spectrum [Fig. 5(b)] can be deconvoluted into three components at binding energies of 283.65, 285.20, and 286.89 eV, which are assigned to C=C/C–C, C—N, and C—O species, respectively. In addition, two peaks located at 280.95 and 284.78 eV are attributed to the Ru $3d_{5/2}$ and Ru $3d_{3/2}$ levels, respectively, which partially overlap with the C 1 s region. To clearly identify the oxidation state of Ru without interference from the C 1 s signal, the Ru 3p core-level spectrum was further analyzed. As shown in Fig. 5(c), the Ru 3p spectrum exhibits two well-resolved peaks at 462.05 and 484.33 eV, corresponding to the Ru^{3+} $3p_{3/2}$ and Ru^{3+} $3p_{1/2}$ states, respectively, confirming the +3-oxidation state of Ru in Ru@PFCTF-10-500. Furthermore, the deconvoluted N 1 s spectrum (Fig. 5(d)) displays peaks at 397.43, 399.58, and 401.78 eV, which are assigned to pyridinic N, pyrrolic N, and quarternary N species, respectively. Notably, an additional peak observed at 398.63 eV is attributed to Ru—N coordination. Collectively, these XPS results provide clear evidence for the successful coordination of Ru species with the pyridinic nitrogen atoms of the triazine framework in Ru@PFCTF-10-500. XRD analysis revealed that both PFCTF-5-500 and PFCTF-10-500 exhibit amorphous characteristics [**Fig. S12**], which is consistent with the observations from the TEM image [Fig. 5(e)]. Morphological analysis by SEM, combined with EDS elemental mapping (Fig. 5(f)), demonstrates that Ru is homogeneously distributed alongside C and N across

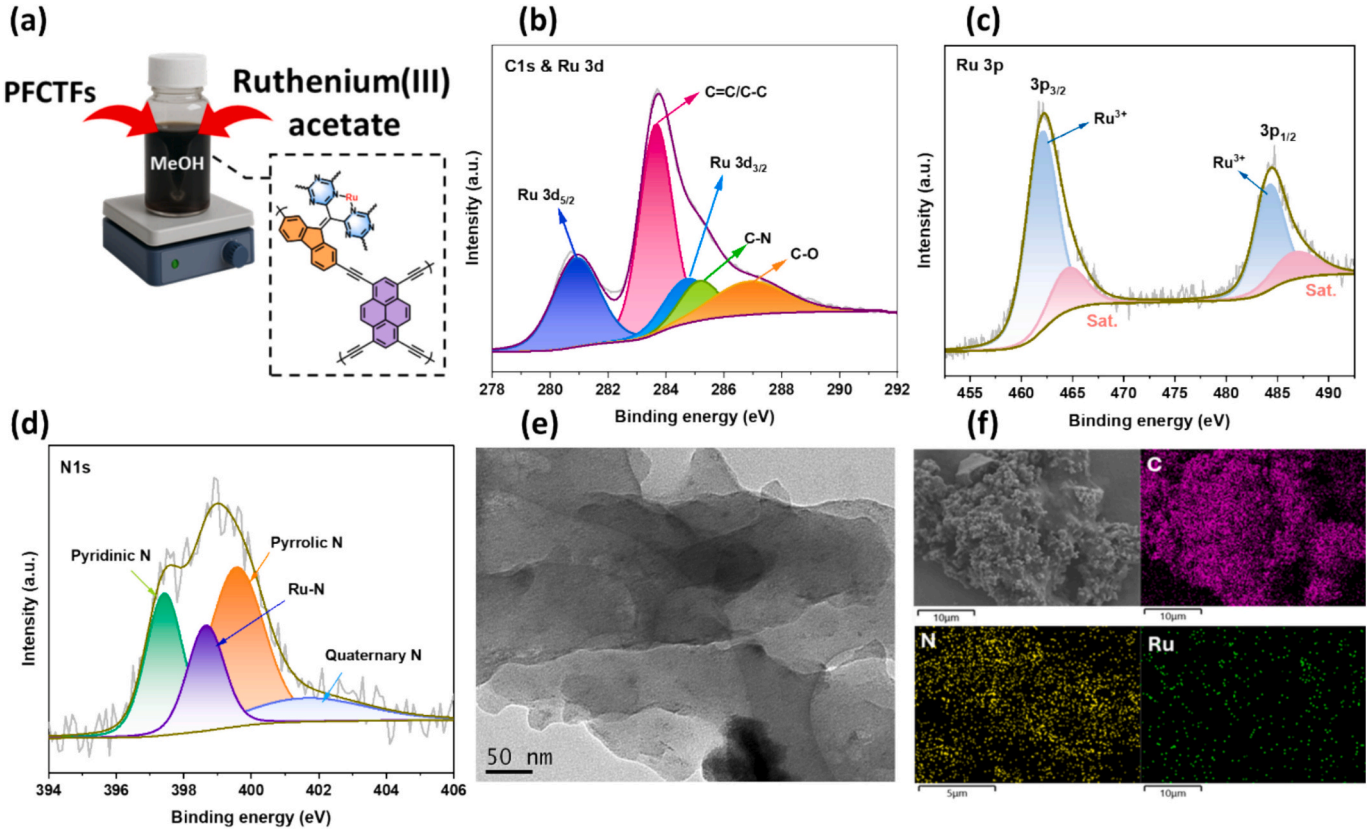

Fig. 5. (a) Synthetic method of Ru@PFCTFs from their corresponding PFCTF precursors, XPS analysis fitting of (b) Ru 3d, (c) Ru 3p, (d) N 1 s, (e) the TEM image, and (f) the SEM image and SEM-EDS elemental mapping images of Ru@PFCTF-10-500.

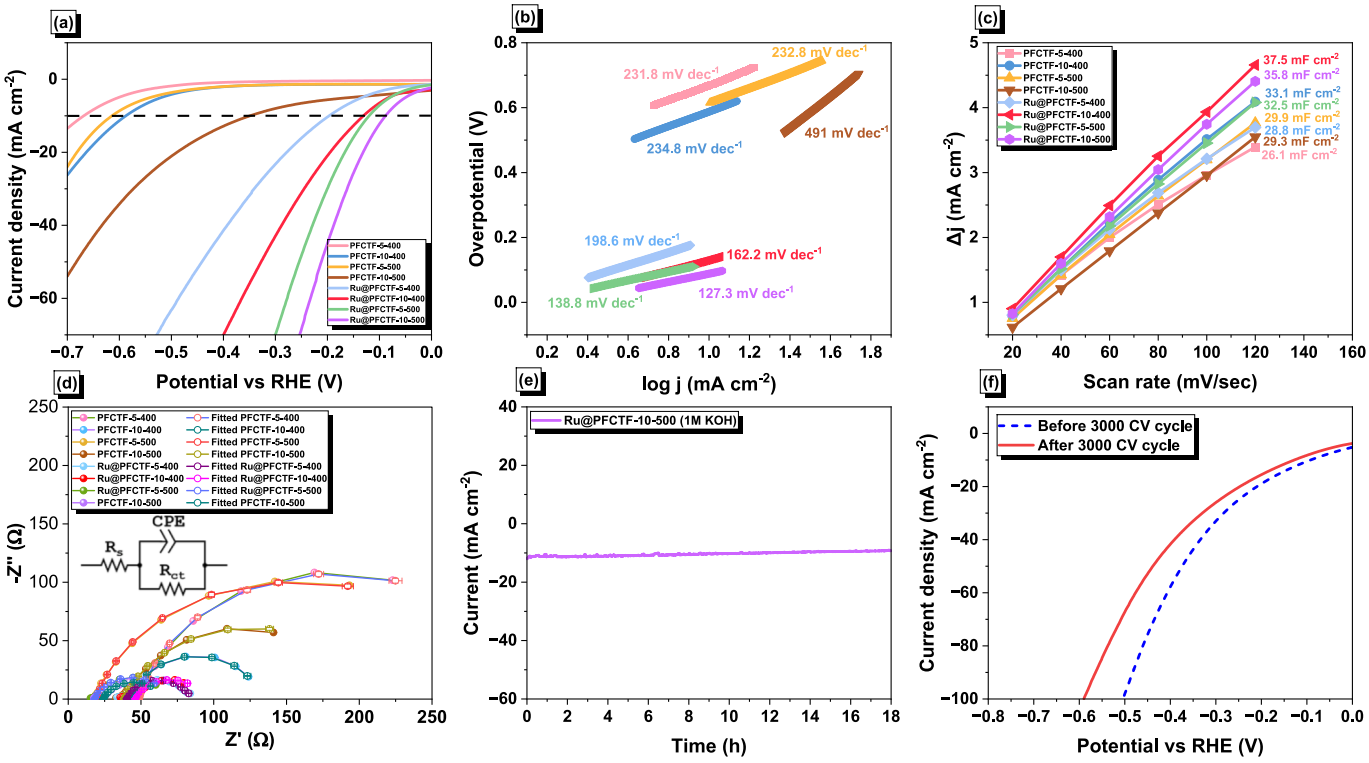

Fig. 6. (a) LSV curves toward electrocatalytic HER of PFCTFs and Ru@PFCTFs, (b) Tafel slope of PFCTFs and Ru@PFCTFs, (c) Linear fitting of Δj ($\Delta j = j_a - j_c$) vs. scan rate at a potential of +0.6 V (vs. RHE). (d) Raw and Fitted Nyquist plots of PFCTFs and Ru@PFCTFs (inset: equivalent Randles circuit, Fitting Error: 2%), (e) Chronopotentiometry measurement of the HER at about 10 mA cm^{-2} for 18 h in 1 M KOH, and (f) LSV curves for Ru@PFCTF-10-500 before and after 3000 CV cycles in 1.0 M KOH solution.

the PFCTF material's surface, with no signs of particle aggregation, underscoring the uniform integration of Ru^{3+} within the PFCTF framework.

The electrocatalytic HER activity of the Ru@PFCTF materials in 1 M KOH was evaluated via linear sweep voltammetry (LSV). As shown in Fig. 6(a), the obtained PFCTFs required overpotentials (η) exceeding 300 mV to achieve a current density of −10 mA cm^{-2}, reflecting poor intrinsic catalytic activity. In sharp contrast, Ru@PFCTF-10-500 delivered an exceptionally low overpotential of 89 mV, highlighting its superior HER activity. In comparison, Ru@PFCTF-5-400, Ru@PFCTF-10-400, and Ru@PFCTF-5-500 exhibited higher overpotentials of 197, 131, and 120 mV, respectively. Moreover, by comparing the LSV data of Pt/C, the Ru@PFCTF-10-500 needed 49 mV more overpotential to deliver −10 mA cm^{-2} current density than that of Pt/C (η_{10} = 40 mV) [**Fig. S13**]. Additionally, the overpotential (η_{10}) of Ru@PFCTF-10-500 is lower than or comparable to those of previously reported metal-coordinated POP-based electrocatalysts, including COFs, CMPs, and MOFs (**Table S4**). Ni@PFCTF-10-500 and Co@PFCTF-10-500 were synthesized using the same procedure as that for Ru@PFCTF-10-500. Their electrocatalytic HER performances were then evaluated in a three-electrode system. As shown in the LSV curves [**Fig. S14**], Ni@PFCTF-10-500 and Co@PFCTF-10-500 require overpotentials of 537 and 502 mV, respectively, to achieve a current density of −10 mA cm^{-2}. In contrast, Ru@PFCTF-10-500 reaches the same current density at a much lower overpotential of only 89 mV. These findings elucidate that Ru is a more effective active site for HER than Co and Ni. Tafel slope analysis (Fig. 6(b)) further revealed the sluggish reaction kinetics of the synthesized PFCTF-5-400, PFCTF-10-400, PFCTF-5-500, and PFCTF-10-500 with slopes of 230.8, 234.8, 232.8, and 490 mV dec^{-1}. In comparison, Ru@PFCTF-5-400, Ru@PFCTF-10-400, Ru@PFCTF-5-500, and Ru@PFCTF-10-500 achieved a slope of 198.6, 162.2, 138.8, and 127.3 mV dec^{-1}, indicative of faster charge-transfer kinetics and consistent with Volmer-dominated rate-determining step (r.d.s) [74]. The lower Tafel slope observed for Ru@PFCTF-10-500 (127.3 mV dec^{-1}) suggests improved electron transfer efficiency and a more favorable HER response [74–77]. Cyclic voltammetry (CV) experiments on PFCTFs and Ru@PFCTFs were carried out in the non-faradaic potential range across various scan rates [**Figs. S15** and **S16**]. The double-layer capacitance (C_{dl}) was obtained by determining the slope of the graph plotting the change in current density (ΔJ) against the scan rate. The electrochemical double-layer capacitance (C_{dl}), a proxy for electrochemically active surface area, is shown in Fig. 6(c). Ru@PFCTF-10-400 and Ru@PFCTF-10-500 samples displayed markedly higher C_{dl} values [37.5 and 35.8 mF cm^{-2}; respectively] than their pristine PFCTF counterparts, confirming a substantial increase in active site density for HER. In addition, the C_{dl}, the turnover frequency (TOF), and mass activity were evaluated to provide a more comprehensive assessment of the HER performance. The TOF values were calculated under alkaline conditions to quantify the intrinsic catalytic activity, as detailed in the Supporting Information. As shown in **Fig. S17(a)**, PFCTF-10-500 exhibits a TOF of 0.92 s^{-1} at an overpotential of 150 mV in a basic electrolyte. Upon Ru ions incorporation, Ru@PFCTF-10-500 delivers a markedly higher TOF of 3.98 s^{-1} under identical conditions, representing an approximately fourfold enhancement compared to the Ru-free counterpart. Furthermore, all Ru-based catalysts (Ru@PFCTF-5-400, Ru@PFCTF-10-400, Ru@PFCTF-5-500, and Ru@PFCTF-10-500) consistently exhibit higher TOF values than their corresponding Ru-free samples (PFCTF-5-400, PFCTF-10-400, PFCTF-5-500, and PFCTF-10-500). These results clearly indicate that Ru incorporation significantly enhances the intrinsic catalytic activity toward HER. To further evaluate the practical catalytic performance, the current density was normalized to the catalyst loading on the glassy carbon electrode (GCE) to determine the mass activity.

As presented in **Fig. S17(b)**, Ru@PFCTF-10-500 achieves a mass activity of 150 A g^{-1} at an overpotential of 190 mV, whereas PFCTF-10-500 requires a substantially higher overpotential of 638 mV to reach the same mass activity. This pronounced enhancement in mass activity demonstrates that Ru incorporation markedly improves the catalytic efficiency per unit mass, underscoring its effectiveness in promoting HER performance. To elucidate the charge-transfer resistance (R_{ct}) at the electrode–electrolyte interface, electrochemical impedance spectroscopy (EIS) measurements were performed for all electrocatalysts at the overpotential of 100 mV. The Nyquist plots were fitted using the Randles equivalent circuit model. As shown in Fig. 6(d), the extracted charge-transfer resistance (R_{ct}) values for PFCTF-5-400, PFCTF-10-400, PFCTF-5-500, PFCTF-10-500, Ru@PFCTF-5-400, Ru@PFCTF-10-400, Ru@PFCTF-5-500, and Ru@PFCTF-10-500 were 270.7, 87.5, 264.2, 175.0, 44.2, 48.4, 52.1, and 41.9 Ω, respectively. The corresponding solution resistance (R_s) values were determined to be 48.5, 44.4, 19.1, 37.9, 40.3, 46.6, 18.8, and 23.9 Ω, respectively. Notably, the Ru@PFCTF-10-500 electrode exhibits the lowest R_{ct} value among all samples, indicating markedly enhanced charge-transfer kinetics at the electrode–electrolyte interface. This improved interfacial electron transport is attributed to the synergistic effect of Ru incorporation and optimized thermal treatment, which collectively facilitate rapid electrochemical reactions. Beyond achieving high HER activity, long-term operational stability is a critical criterion for evaluating the practical reliability of electrocatalysts. Accordingly, the durability of Ru@PFCTF-10-500 was assessed via chronoamperometric (i–t) stability measurements. An 18 h test conducted at a constant overpotential of 130 mV (vs. RHE) revealed that Ru@PFCTF-10-500 retained approximately 77% of its initial current density, indicating good steady-state catalytic durability [Fig. 6(e)] [**78**]. Furthermore, extended i–t stability testing for up to 100 h at a constant potential of −0.23 V (vs. RHE) demonstrated a nearly constant current response, further confirming the excellent long-term electrochemical stability of Ru@PFCTF-10-500 [**Fig. S18**]. To further examine the structural and electrochemical robustness of the catalyst, linear sweep voltammetry (LSV) curves were recorded before and after 3000 CV cycles [Fig. 6(f)]. After cycling, only a modest increase of 33 mV in the overpotential required to achieve a current density of −10 mA cm^{-2} was observed, underscoring the strong electrochemical durability and robustness of Ru@PFCTF-10-500. Additionally, to verify the stability of Ru during long-term electrochemical operation, inductively coupled plasma-optical emission spectroscopy (ICP-OES) analysis was performed on the electrolyte after the stability test. The ICP-OES results of the electrolyte after a 100 h chronoamperometric stability test of Ru@PFCTF10–500 revealed no detectable Ru leaching, confirming the excellent coordination stability of Ru within the PFCTF framework. Following the 100 h chronoamperometric stability test, the structural and morphological integrity of Ru@PFCTF-10-500 was further investigated using SEM and TEM [**Fig. S19**]. The TEM analysis reveals that Ru@PFCTF-10-500 preserves its amorphous structural characteristics even after prolonged electrochemical operation for 100 h, indicating excellent structural stability under alkaline HER conditions. In addition, the SEM images [**Fig. S19**] confirm that the characteristic spherical aggregate morphology of Ru@PFCTF-10-500 remains essentially unchanged after extended alkaline HER testing, demonstrating the robust morphological durability of the catalyst during long-term electrochemical operation. These results collectively confirm the exceptional structural robustness and enduring HER activity of the catalyst under prolonged alkaline operation. **Fig. S20** and **Table S4** present a comprehensive comparison of the HER performance of Ru@PFCTF catalysts with various benchmark materials. The results highlight Ru@PFCTF-10-500 as a top-performing electrocatalyst for HER, which can be attributed to a combination of favorable structural, electronic, and interfacial properties. First, the relatively high specific surface area of Ru@PFCTF-10-500 provides abundant accessible active sites, thereby increasing the number of electrochemically available Ru centers and facilitating efficient contact between the catalyst surface and the electrolyte. This structural advantage significantly enhances the intrinsic catalytic activity by promoting rapid adsorption of reactant species. In addition, the elevated content of pyridinic nitrogen within the Ru@PFCTF-10-500 framework plays a crucial role in

modulating the electronic structure of the anchored Ru species. Pyridinic N atoms can act as strong coordination sites, stabilizing Ru atoms and clusters through Ru—N interactions while simultaneously tuning the local electron density. This electronic modulation improves hydrogen adsorption energetics and accelerates interfacial charge transfer during HER. Moreover, the strong coupling between Ru species and the nitrogen-rich carbon framework contributes to the excellent electrochemical stability of the catalyst under alkaline conditions. Electrochemical impedance spectroscopy further supports this interpretation, as Ru@PFCTF-10-500 exhibits a low R_{ct}, indicating fast electron transport across the catalyst–electrolyte interface. The reduced R_{ct} reflects enhanced electrical conductivity and efficient electron delivery to the active sites, which is essential for sustaining high HER rates. Furthermore, the relatively low Tafel slope observed for Ru@PFCTF-10-500 (127.3 mV dec^{-1}) suggests improved HER kinetics and a more favorable reaction pathway. Such a Tafel slope is indicative of a Volmer step–limited process, implying that the initial electrochemical discharge of water molecules is the rate-determining step. This behavior is consistent with enhanced electron transfer efficiency and optimized surface energetics for hydrogen adsorption. Furthermore, the catalytic HER activity of all samples was evaluated in a 0.5 M H_2SO_4 electrolyte. The corresponding LSV curves are presented in **Fig. S21**. The results demonstrate that the incorporation of Ru significantly lowers the overpotentials of the PFCTF-based catalysts compared with the pristine PFCTFs, indicating enhanced proton reduction efficiency. Among the catalysts, Ru@PFCTF-10-500 exhibits the best performance, requiring an overpotential of only 143 mV to achieve a current density of −10 mA cm^{-2} [**Fig. S21**]. In contrast, Ru@PFCTF-5-400, Ru@PFCTF-10-400, and Ru@PFCTF-5-500 require higher overpotentials of 271, 262, and 229 mV, respectively. Notably, the Ru-free PFCTF-5-400, PFCTF-10-400, PFCTF-5-500, and PFCTF-10-500 display much higher overpotentials of 736, 560, 622, and 383 mV, respectively, at a current density of −10 mA cm^{-2}.

4. Conclusion

The malononitrile-functionalized CMP [PF-CN CMP] was successfully transformed into PFCTFs featuring triazine rings via ionothermal reactions at 400 °C and 500 °C. The resulting materials show great promise as adsorbents and catalysts for gas capture and electrocatalytic H_2 production, respectively. BET and TGA analyses confirmed significant improvements in pore structure and thermal stability, attributed to the combined effects of high surface area, nanoporous architecture, and nitrogen-containing functionalities. Notably, PFCTF-10-500 exhibited excellent CO_2 adsorption, reaching a maximum uptake of 5.73 mmol g^{-1} at 1 bar and 273 K. Moreover, the electrocatalytic performance was markedly enhanced by nitrogen atoms in the PFCTF frameworks coordinating with Ru^{3+} metal ions. The Ru@PFCTF-10-500 catalyst exhibited HER activity, achieving a low overpotential of 89 mV, a Tafel slope of 127.3 mV dec^{-1}, and a higher electrochemical C_{dl} of 35.8 mF cm^{-2}, indicative of faster charge-transfer kinetics and a more favorable HER mechanism. This innovative approach for synthesizing CTF materials from CMP precursors not only delivers exceptional CO_2 capture and enhanced HER performance but also provides a powerful strategy to finely tune the pore architecture of porous organic polymers (POPs), thereby advancing the development of next-generation nanoporous materials with tailored functionalities.

CRediT authorship contribution statement

Mohamed Gamal Mohamed: Writing – review & editing, Writing – original draft, Supervision, Methodology, Investigation, Formal analysis, Data curation, Conceptualization. **Nian-Ping Chen:** Formal analysis, Data curation, Conceptualization. **Tapomay Mondal:** Data curation, Formal analysis. **Shiao-Wei Kuo:** Supervision, Resources.

Declaration of competing interest

The authors declare that they have no known competing financial interests or personal relationships that could have appeared to influence the work reported in this paper.

Acknowledgments

This study was supported financially by the National Science and Technology Council, Taiwan, under contracts NSTC 114-2223-E-110-001- and 113-2221-E-110-012-MY3. The authors thank the staff at National Sun Yat-sen University for their assistance with the TEM (ID: EM022600) experiments.

Appendix A. Supplementary data

Supplementary data to this article can be found online at https://doi.org/10.1016/j.seppur.2026.137008.

Data availability

Data will be made available on request.

References

[1] H. Han, Z. Zeeshan, B.A. Talpur, T. Sadiq, U.A. Bhatti, E.M. Awwad, M. Al-Razgan, Y.Y. Ghadi, Studying long term relationship between carbon emissions, soil, and climate change: insights from a global earth modeling framework, Int. J. Appl. Earth Obs. Geoinf. 130 (2024) 103902, https://doi.org/10.1016/j.jag.2024.103902.
[2] M.G. Mohamed, S.Y. Chang, M. Ejaz, M.M. Samy, A.O. Mousa, S.W. Kuo, Design and synthesis of bisulfone-linked two-dimensional conjugated microporous polymers for CO_2 adsorption and energy storage, Molecules 28 (2023) 3234, https://doi.org/10.3390/molecules28073234.
[3] Y. Dai, Z. Niu, Y. Wang, S. Zhong, P. Mu, J. Li, Recent advances and prospect of emerging microporous membranes for high-performance CO_2 capture, Sep. Purif. Technol. 318 (2023) 123992, https://doi.org/10.1016/j.seppur.2023.123992.
[4] E. Sivasurya, R. Atchudan, M.G. Mohamed, A. Thangamani, S. Rajendran, A. Jalil, P.K. Kalambate, D. Manoj, S.W. Kuo, Electrocatalytic conversion of CO_2 into selective carbonaceous fuels using metal-organic frameworks: An overview of recent progress and perspectives, Mater. Today Chem. 44 (2025) 102538, https://doi.org/10.1016/j.mtchem.2025.102538.
[5] M.G. Mohamed, C.C. Chen, K. Zhang, S.W. Kuo, Construction of three-dimensional porous organic polymers with enhanced CO_2 uptake performance via solid-state thermal conversion from tetrahedral benzoxazine-linked precursor, Eur. Polym. J. 200 (2023) 112551, https://doi.org/10.1016/j.eurpolymj.2023.112551.
[6] M. Filonchyk, M.P. Peterson, L. Zhang, V. Hurynovich, Y. He, Greenhouse gases emissions and global climate change: examining the influence of CO_2, CH_4, and N_2O, Sci. Total Environ. 935 (2024) 173359, https://doi.org/10.1016/j.scitotenv.2024.173359.
[7] M. Ejaz, M.G. Mohamed, S.W. Kuo, Benzoxazine-linked polyhedral oligomeric silsesquioxane: 3D porous organic-inorganic polymer for improved CO_2 capture and supercapacitor performance, J. Taiwan Inst. Chem. Eng. (2025) 106098, https://doi.org/10.1039/D3PY00158J.
[8] Y.C. Kao, K.T. Yeh, M.G. Mohamed, H. Karim, W.H. Su, S.W. Kuo, Structural modulation via mesoporous silica templating in covalent organic frameworks: converting functional aspects for adsorption behavior, Sep. Purif. Technol. 357 (2025) 133827, https://doi.org/10.1016/j.seppur.2025.133827.
[9] S.O. Akpasi, I.M.S. Anekwe, E.K. Tetteh, U.O. Amune, S.I. Mustapha, S.L. Kiambi, Hydrogen as a clean energy carrier: advancements, challenges, and its role in a sustainable energy future, Clean Energy 9 (2025) 52–88, https://doi.org/10.1093/ce/zkae112.
[10] M.G. Mohamed, C.C. Chen, M. Ibrahim, A.O. Mousa, M.H. Elsayed, Y. Ye, S.W. Kuo, Tetraphenylanthraquinone and dihydroxybenzene-tethered conjugated microporous polymer for enhanced CO_2 uptake and supercapacitive energy storage, JACS Au 4 (2024) 3593–3605, https://doi.org/10.1021/jacsau.4c00537.
[11] S. Das, P. Sharma, M. Kumar, R.K. Gupta, H. Sharma, A review on clay exfoliation methods and modifications for CO_2 capture application, Mater. Today Sustain. 23 (2023) 100427, https://doi.org/10.1016/j.mtsust.2023.100427.
[12] D. Song, F. Jiang, D. Yuan, Q. Chen, M. Hong, Optimizing sieving effect for CO_2 capture from humid air using an adaptive Ultramicroporous framework, Small 19 (2023) 2302677, https://doi.org/10.1002/smll.202302677.
[13] S. Zhong, X. Guo, A. Zhou, Z. Chen, D. Jin, M. Fan, T. Ma, Fundamentals and recent Progress in magnetic field assisted CO_2 capture and conversion, Small 20 (2024) 2305533, https://doi.org/10.1002/smll.202305533.
[14] T. Li, X. An, D. Fu, Review on nitrogen-doped porous carbon materials for CO_2 adsorption and separation: recent advances and outlook, Energy Fuel 37 (2023) 8160–8179, https://doi.org/10.1021/acs.energyfuels.3c00941.

[15] M.G. Mohamed, C.C. Chen, S.W. Kuo, Nitrogen and sulfur co-doped microporous carbon through benzo[c]-1,2,5-thiadiazole-functionalized benzoxazine-linkage porous organic polymer in CO_2 capture and energy storage, React. Funct. Polym. 214 (2025) 106286, https://doi.org/10.1016/j.reactfunctpolym.2025.106286.

[16] S. Dai, P. Shen, W. Deng, Q. Yu, Hydrogen energy in electrical power systems: A review and future outlook, Electronics 13 (2024) 3370, oi.org/10.3390/electronics13173370.

[17] T.T. Le, P. Sharma, B.J. Bora, V.D. Tran, T.H. Truong, H.C. Le, P.Q.P. Nguyen, Fueling the future: A comprehensive review of hydrogen energy systems and their challenges, Int. J. Hydrog. Energy 54 (2024) 791–816, https://doi.org/10.1016/j.ijhydene.2023.08.044.

[18] E.A. Hamedani, S.A. Alenabi, S. Talebi, Hydrogen as an energy source: A review of production technologies and challenges of fuel cell vehicles, Energy Rep. 12 (2024) 3778–3794, https://doi.org/10.1016/j.egyr.2024.09.030.

[19] A.A. Feidenhans'l, Y.N. Regmi, C. Wei, D. Xia, J. Kibsgaard, L.A. King, Precious metal-free hydrogen evolution catalyst design and application, Chem. Rev. 124 (2024) 5617–5667, https://doi.org/10.1021/acs.chemrev.3c00712.

[20] M.A. Qadeer, X. Zhang, M.A. Farid, M. Tanveer, Y. Yan, S. Du, Z.F. Huang, M. Tahir, J.J. Zou, A review on fundamentals for designing hydrogen evolution electrocatalyst, J. Power Sources 613 (2024) 234856, https://doi.org/10.1016/j.jpowsour.2024.234856.

[21] J.N. Hansen, H. Prats, K.K. Toudahl, N.M. Secher, K. Chan, J. Kibsgaard, I. Chorkendorff, I., Is there anything better than pt for HER? ACS Energy Lett. 6 (2021) 1175–1180, https://doi.org/10.1021/acsenergylett.1c00246.

[22] L. Liang, H. Jin, H. Zhou, B. Liu, C. Hu, D. Chen, Z. Wang, Z. Hu, Y. Zhao, H.W. Li, Cobalt single atom site isolated pt nanoparticles for efficient ORR and HER in acid media, Nano Energy 88 (2021) 106221, https://doi.org/10.1016/j.nanoen.2021.106221.

[23] H. Haridas, B. Somapur, H.S. Akkera, N. Neella, N. Kambhala, Review on recent advances of nickel Sulfide Nano electrocatalysts for hydrogen evolution, ChemistrySelect 9 (2024) 202402550, https://doi.org/10.1002/slct.202402550.

[24] J. Hu, C. Zhang, X. Meng, H. Lin, C. Hu, X. Long, S. Yang, Hydrogen evolution electrocatalysis with binary-nonmetal transition metal compounds, J. Mater. Chem. A 5 (2017) 5995–6012, https://doi.org/10.1039/C7TA00743D.

[25] Z. Chen, X. Duan, W. Wei, S. Wang, B.J. Ni, Recent advances in transition metal-based electrocatalysts for alkaline hydrogen evolution, J. Mater. Chem. A 7 (2019) 14971–15005, https://doi.org/10.1039/C9TA03220G.

[26] W. Zhou, J. Jia, J. Lu, L. Yang, D. Hou, G. Li, S. Chen, Recent developments of carbon-based electrocatalysts for hydrogen evolution reaction, Nano Energy 28 (2016) 29–43, https://doi.org/10.1016/j.nanoen.2016.08.027.

[27] L. Zhang, J. Xiao, H. Wang, M. Shao, Carbon-based electrocatalysts for hydrogen and oxygen evolution reactions, ACS Catal. 7 (2017) 7855–7865, https://doi.org/10.1021/acscatal.7b02718.

[28] I.M.A. Mekhemer, A.M. Elewa, M.M. Elsenety, M.M. Samy, M.G. Mohamed, A. F. Musa, T.F. Huang, T.C. Wei, S.W. Kuo, B.H. Chen, S.D. Yang, H.H. Chou, Self-condensation for enhancing the hydrophilicity of covalent organic polymers and photocatalytic hydrogen generation with unprecedented apparent quantum yield up to 500 nm, Chem. Eng. J. 497 (2024) 154280, https://doi.org/10.1016/j.cej.2024.154280.

[29] I.M.A. Mekhemer, M. Elsenety, A. Elewa, K.D.G. Huynh, M.M. Samy, M. G. Mohamed, D.M. Dorrah, D.C.K. Hoang, A.F. Musa, S.W. Kuo, H.H. Chou, Push-pull-pull interactions of 2D imide-imine based covalent organic framework to promote charge separation in photocatalytic hydrogen production, J. Mater. Chem. A 12 (2024) 10790–10798, https://doi.org/10.1016/j.ccr.2023.215066.

[30] M.M. Samy, I.M.A. Mekhemer, M.G. Mohamed, M.H. Elsayed, K.H. Lin, Y.K. Chen, T.L. Wu, H.H. Chou, S.W. Kuo, Conjugated microporous polymers incorporating Thiazolo [5,4-d] thiazole moieties for sunlight-driven hydrogen production from water, Chem. Eng. J. 446 (2022) 137158, https://doi.org/10.1016/j.cej.2022.137158.

[31] W.T. Chung, I.M.A. Mekhemer, M.G. Mohamed, A.M. Elewa, A.F.M. EL-Mahdy, H. H. Chou, S.W. Kuo, K.C.W. Wu, Recent advances in metal/covalent organic frameworks based materials: their synthesis, structure design and potential applications for hydrogen production, Coord. Chem. Rev. 483 (2023) 215066, https://doi.org/10.1016/j.ccr.2023.215066.

[32] M.G. Mohamed, M.H. Elsayed, C.J. Li, A.E. Hassan, I.M.A. Mekhemer, A.F. Musa, M.K. Hussien, L.C. Chen, K.H. Chen, H.H. Chou, S.W. Kuo, Reticular design and alkyne bridge engineering in donor–π–acceptor type conjugated microporous polymers for boosting photocatalytic hydrogen evolution, J. Mater. Chem. A 12 (2024) 7693–7710, https://doi.org/10.1039/D3TA07309B.

[33] M.G. Mohamed, I.M.A. Mekhemer, A.F.H. Selim, A. Katsamitros, D. Tasis, A. Basit, H.H. Chou, S.W. Kuo, Molecular engineering of donor–acceptor-type conjugated microporous polymers for dual effective photocatalytic production of hydrogen and hydrogen peroxide, Mater. Horiz. 12 (2025) 5917–5928, https://doi.org/10.1039/D5MH00735F.

[34] M. Jahan, Z. Liu, K.P. Loh, A graphene oxide and copper-centered metal organic framework composite as a tri-functional catalyst for HER, OER, and ORR, Adv. Funct. Mater. 23 (2013) 5363–5372, https://doi.org/10.1002/adfm.201300510.

[35] Z. Chen, H. Qing, K. Zhou, D. Sun, R. Wu, Metal-organic framework-derived nanocomposites for electrocatalytic hydrogen evolution reaction, Prog. Mater. Sci. 108 (2020) 100618, https://doi.org/10.1016/j.pmatsci.2019.100618.

[36] B. Zhu, R. Zou, Q. Xu, Metal–organic framework-based catalysts for hydrogen evolution, Adv. Energy Mater. 8 (2018) 1801193, https://doi.org/10.1002/aenm.201801193.

[37] N. Wang, J. Zhou, J. Ren, Recent advances in CO_2 capture and utilization, Renew. Sust. Energ. Rev. 216 (2025) 115688, https://doi.org/10.1016/j.rser.2025.115688.

[38] A. Badreldin, Y. Li, A critical appraisal of advances in integrated CO_2 capture and electrochemical conversion, Chem. Sci. 16 (2025) 2483–2513, https://doi.org/10.1039/D4SC06642A.

[39] Q. Wang, Z. Fang, W. Zhang, D. Zhang, High-efficiency g-C_3N_4 based photocatalysts for CO_2 reduction: modification methods, Adv. Fiber Mater. 4 (2022) 342–360, https://doi.org/10.1007/s42765-021-00122-7.

[40] A. Raveendran, M. Chandran, R. Dhanusuraman, A comprehensive review on the electrochemical parameters and recent material development of electrochemical water splitting electrocatalysts, RSC Adv. 13 (2023) 3843–3876, https://doi.org/10.1039/D2RA07642J.

[41] K. Jung, D.S.A. Pratama, A. Haryanto, J.I. Jang, H.M. Kim, J.C. Kim, C.W. Lee, D. W. Kim, Iridium-cluster-implanted ruthenium phosphide electrocatalyst for hydrogen evolution reaction, Adv. Fiber Mater. 6 (2024) 158–169, https://doi.org/10.1007/s42765-023-00342-z.

[42] O.H.P. Gunawardene, C.A. Gunathilake, K. Vikrant, S.M. Amaraweera, Carbon dioxide capture through physical and chemical adsorption using porous carbon materials: A review, Atmosphere 13 (2022) 397, https://doi.org/10.3390/atmos13030397.

[43] S. Aslam, S. Rani, K. Lal, M. Fatima, T. Hardwick, B. Shirinfar, N. Ahmed, Electrochemical hydrogen production: sustainable hydrogen economy, Green Chem. 25 (2023) 9543–9573, https://doi.org/10.1039/D3GC02849F.

[44] M.G. Mohamed, B.X. Su, S.W. Kuo, Robust nitrogen-doped microporous carbon via crown ether-functionalized benzoxazine-linked porous organic polymers for enhanced CO_2 adsorption and supercapacitor applications, ACS Appl. Mater. Interfaces 16 (2024) 40858–40872, https://doi.org/10.1021/acsami.4c05645.

[45] S.Y. Chang, A.M. Elewa, M.G. Mohamed, I.M.A. Mekhemer, M.M. Samy, K. Zhang, H.H. Chou, S.W. Kuo, Rational design and synthesis of bifunctional Dibenzo[g,p] chrysene-based conjugated microporous polymers for energy storage and visible light-driven photocatalytic hydrogen evolution, Mater. Today Chem. 33 (2023) 101680, https://doi.org/10.1016/j.mtchem.2023.101680.

[46] M.G. Mohamed, A.F.M. EL-Mahdy, M.G. Kotp, S.W. Kuo, Advances in porous organic polymers: syntheses, structures, and diverse applications, Mater. Adv. 3 (2022) 707–733, https://doi.org/10.1039/D1MA00771H.

[47] J.S.M. Lee, A.I. Cooper, Advances in conjugated microporous polymers, Chem. Rev. 120 (2020) 2171–2214, https://doi.org/10.1021/acs.chemrev.9b00399.

[48] Y. Xu, S. Jin, H. Xu, A. Nagai, D. Jiang, Conjugated microporous polymers: design, synthesis and application, Chem. Soc. Rev. 42 (2013) 8012–8031, https://doi.org/10.1039/c3cs60160a.

[49] H. Wang, G. Wang, L. Hu, B. Ge, X. Yu, J. Deng, Porous polymer materials for CO_2 capture and electrocatalytic reduction, Materials 16 (2023) 1630, https://doi.org/10.3390/ma16041630.

[50] S.Y. Liu, M. Pachaiyappan, Innovative approaches in molecular design, synthesis, and functionalization of conjugated organic polymer (D-A, D-π-A, A-A-D, A-D-A) photocatalysts for sustainable green hydrogen production, J. Mater. Chem. A 13 (2025) 30870–30905, https://doi.org/10.1039/D5TA04101E.

[51] H. Ali, O. Iqbal, M. Sadiq, Y. Cheng, X. Yan, B. Al Alwan, A. El Jery, H. Ur Rahman, Y. Qian, A. Hayat, D. Yue, Z. Ajmal, Novel advancements in synthesis, modulation, and potential applications of conjugated microporous polymer-based materials. Nano, Mater. Sci. (2025), https://doi.org/10.1016/j.nanoms.2024.08.008.

[52] M.G. Mohamed, M.H. Elsayed, A.M. Elewa, A.F.M. EL-Mahdy, C.H. Yang, A.A. K. Mohammed, H.H. Chou, S.W. Kuo, Pyrene-containing conjugated organic microporous polymers for photocatalytic hydrogen evolution from water, Cat. Sci. Technol. 11 (2021) 2229–2241, https://doi.org/10.1039/D0CY02482A.

[53] L. Liao, M. Li, Y. Yin, J. Chen, Q. Zhong, R. Du, S. Liu, Y. He, W. Fu, F. Zeng, Advances in the synthesis of covalent triazine frameworks, ACS Omega 8 (2023) 4527–4542, https://doi.org/10.1021/acsomega.2c06961.

[54] Y. Ren, S. Yang, Y. Xu, Crystalline covalent triazine frameworks and 2D triazine polymers: synthesis and applications, Acc. Chem. Res. 58 (2025) 474–487, https://doi.org/10.1021/acs.accounts.4c00729.

[55] Z. Qian, Z.J. Wang, K.A.I. Zhang, Covalent triazine frameworks as emerging heterogeneous photocatalysts, Chem. Mater. 33 (2021) 1909–1926, https://doi.org/10.1021/acs.chemmater.0c04348.

[56] Y. Zheng, N.A. Khan, X. Ni, K.A.I. Zhang, Y. Shen, N. Huang, X.Y. Kong, L. Ye, Emerging covalent triazine framework-based nanomaterials for electrochemical energy storage and conversion, Chem. Commun. 59 (2023) 6314–6334, https://doi.org/10.1039/D3CC00712J.

[57] Y. Chen, X. Hu, J. Guo, Z. Guo, H. Zhan, S. Du, Optimizing CO_2 capture and separation in pyrene-derived covalent triazine frameworks, Eur. Polym. J. 171 (2022) 111215, https://doi.org/10.1016/j.eurpolymj.2022.111215.

[58] Y. Zhao, Y. Liang, D. Wu, H. Tian, T. Xia, W. Wang, W. Xie, X.M. Hu, X. Tian, Q. Chen, Q., Ruthenium complex of sp^2 carbon-conjugated covalent organic frameworks as an efficient electrocatalyst for hydrogen evolution, Small 18 (2022) 2107750, https://doi.org/10.1002/smll.202107750.

[59] M.G. Mohamed, W.C. Chang, S.W. Kuo, Crown ether- and benzoxazine-linked porous organic polymers displaying enhanced metal ion and CO_2 capture through solid-state chemical transformation, Macromolecules 55 (2022) 7879–7892, https://doi.org/10.1021/acs.macromol.2c01216.

[60] M.G. Mohamed, T.C. Chen, S.W. Kuo, Solid-state chemical transformations to enhance gas capture in benzoxazine-linked conjugated microporous polymers, Macromolecules 54 (2021) 5866–5877, https://doi.org/10.1021/acs.macromol.1c00736.

[61] M.G. Mohamed, A.M. Elewa, N.P. Chen, A.A.K. Mohammed, S.W. Kuo, Construction of malononitrile-functionalized conjugated microporous polymers as adsorbents for effective adsorption of Rhodamine B and density functional theory perspective, Colloids Surf. A, Physicochem. Eng. Aspects. 721 (2025) 137214, https://doi.org/10.1016/j.colsurfa.2025.137214.

[62] A.O. Mousa, S.U. Sharma, S.V. Chaganti, T.H. Mansoure, P.N. Singh, M. Ejaz, C. H. Chuang, J.T. Lee, S.W. Kuo, M.G. Mohamed, Designing strategically functionalized conjugated microporous polymers with pyrene and perylenetetracarboxylic dianhydride moieties with single-walled carbon nanotubes to enhance supercapacitive energy storage efficiency, J. Power Sources 608 (2024) 234624, https://doi.org/10.1016/j.jpowsour.2024.234624.
[63] C. Chakraborty, M.K. Bera, U. Rana, S. Malik, Vice-versa donor acceptor fluorene-ferrocene alternate copolymer: A twisted ribbon for electrical switching, Chem. Commun. 51 (2015) 13123–13126, https://doi.org/10.1039/C5CC04275E.
[64] M.C. Lin, S.W. Kuo, M.G. Mohamed, High-performance anthracene-linked covalent triazine frameworks with dual functions for CO_2 capture and supercapacitor applications, Mater. Adv. 5 (2024) 6222–6233, https://doi.org/10.1039/D4MA00565A.
[65] M.G. Mohamed, S.U. Sharma, N.Y. Liu, T.H. Mansoure, M.M. Samy, S.V. Chaganti, Y.L. Chang, J.T. Lee, S.W. Kuo, Ultrastable covalent triazine organic framework based on anthracene moiety as platform for high-performance carbon dioxide adsorption and supercapacitors, Int. J. Mol. Sci. 23 (2022) 3174, https://doi.org/10.3390/ijms23063174.
[66] G. Wang, K. Leus, S. Zhao, P.V.D. Voort, Newly designed covalent triazine framework based on novel N-heteroaromatic building blocks for efficient CO_2 and H_2 capture and storage, ACS Appl. Mater. Interfaces 10 (2018) 1244–1249, https://doi.org/10.1021/acsami.7b16239.
[67] M.G. Mohamed, A.F.M. EL-Mahdy, M.M.M. Ahmed, S.W. Kuo, Direct synthesis of microporous Bicarbazole-based covalent triazine frameworks for high-performance energy storage and carbon dioxide uptake, ChemPlusChem 84 (2019) 1767–1774, https://doi.org/10.1002/cplu.201900635.
[68] M.G. Mohamed, A.F.M. EL-Mahdy, Y. Takashi, S.W. Kuo, Ultrastable conductive microporous covalent triazine frameworks based on pyrene moieties provide high-performance CO_2 uptake and supercapacitance, New J. Chem. 44 (2020) 8241–8253, https://doi.org/10.1039/D0NJ01292K.
[69] D.J. Babu, M. Bruns, R. Schneider, D. Gerthsen, J.J. Schneider, Understanding the influence of N-doping on the CO_2 adsorption characteristics in carbon nanomaterials, J. Phys. Chem. C 121 (2017) 616–626, https://doi.org/10.1021/acs.jpcc.6b11686.
[70] D. Li, Y. Chen, M. Zheng, H. Zhao, Y. Zhao, Z. Sun, Hierarchically structured porous nitrogen-doped carbon for highly selective CO_2 capture, ACS Sustain. Chem. Eng. 4 (2016) 298–304, https://doi.org/10.1021/acssuschemeng.5b01230.
[71] M. Ejaz, M.G. Mohamed, Y.T. Chen, K. Zhang, S.W. Kuo, Porous carbon materials augmented with heteroatoms derived from hyperbranched biobased benzoxazine resins for enhanced CO_2 adsorption and exceptional supercapacitor performance, J. Energy Storage 78 (2024) 110166, https://doi.org/10.1016/j.est.2023.110166.
[72] Á.V. Vidal, C.S. López, O.N. Faza, Nitrogen doped nanohoops as promising CO_2 capturing devices, Phys. Chem. Chem. Phys. 20 (2018) 8607–8615, https://doi.org/10.1039/c7cp08498f.
[73] T. Mondal, M.G. Mohamed, A.A.K. Mohamed, S.W. Kuo, Construction of metal-coordinated bipyridine-based conjugated microporous polymers as robust electrocatalysts for hydrogen evolution, ACS Appl. Energy Mater. 8 (2025) 7703–7713, https://doi.org/10.1021/acsaem.5c00992.
[74] A. Wang, L. Cheng, W. Zhao, X. Shen, W. Zhu, Electrochemical hydrogen and oxygen evolution reactions from a cobalt-porphyrin-based covalent organic polymer, J. Colloid Interface Sci. 579 (2020) 598–606, https://doi.org/10.1016/j.jcis.2020.06.109.
[75] L. Rademacher, T.H.Y. Beglau, B. Ali, L. Sondermann, T. Strothmann, I. Boldog, J. Barthel, C. Janiak, Ruthenium nanoparticles on covalent triazine frameworks incorporating thiophene for the electrocatalytic hydrogen evolution reaction, J. Mater. Chem. A 12 (2024) 2093–2109, https://doi.org/10.1039/D3TA05597C.
[76] Y.C. Kao, T. Mondal, W.H. Chang, M.G. Mohamed, S.W. Kuo, Structural tailoring of metal-coordinated salen-tetraphenylethene-based conjugated microporous polymers for superior active alkaline oxygen evolution electrocatalysis, Int. J. Hydrog. Energy 173 (2025) 151390, https://doi.org/10.1016/j.ijhydene.2025.151390.
[77] S.E. Islam, D.R. Hang, C.T. Liang, K.H. Sharma, H.C. Huang, M.M.C. Chou, Tuning the electrocatalytic activity of MoS_2 nanosheets via the in situ hybridization with ruthenium and graphene network, Chem. Eng. J. 488 (2024) 150950, https://doi.org/10.1016/j.cej.2024.150950.